MGD Unstructured Application to a Blunt Body in Two-Dimensions

EDISSON SÁVIO DE GÓES MACIEL
IEA – Aeronautical Engineering Division
ITA – Aeronautical Technological Institute
Praça Mal.do Ar Eduardo Gomes, 50 – Vila das Acácias – São José dos Campos – SP – 12228-900
BRAZIL
edisavio@edissonsavio.eng.br

Abstract: - In this paper, the Euler and Navier-Stokes equations are solved, according to a finite volume formulation and symmetrical unstructured discretization, applied to the problem of a blunt body in two-dimensions. The work of Gaitonde is the reference one to present the fluid dynamics and Maxwell equations of electromagnetism based on a conservative and finite volume formalisms. The Jameson and Mavriplis symmetrical scheme is applied to solve the conserved equations. Two types of numerical dissipation models are applied, namely: Mavriplis and Azevedo. A spatially variable time step procedure is employed aiming to accelerate the convergence of the numerical schemes to the steady state solution. Effective gains in terms of convergence acceleration are observed with this technique (see Maciel). The results have proved that, when the Jameson and Mavriplis scheme is employed with an unstructured alternated discretization, better contours of proprieties are obtained (see Maciel). Moreover, an increase in the shock standoff distance is observed, which guarantees a minor increase in the temperature at the blunt body nose (minor armour problems), and a minor increase in the drag aerodynamic coefficient.

Key-Words: Euler and Navier-Stokes equations, Magnetogasdynamics formulation, Jameson and Mavriplis algorithm, Unstructured spatial discretization, Finite volumes, Two-dimensional space.

1 Introduction

The effects associated with the interaction of magnetic forces with conducting fluid flows have been profitably employed in several applications related to nuclear and other ([1]) technologies and are known to be essential in the explanation of astrophysical phenomena. In recent years, however, the study of these interactions has received fresh impetus in the effort to solve the problems of high drag and thermal loads encountered in hypersonic flight. The knowledge that electrical and magnetic forces can have profound influence on hypersonic flowfields is not new ([2] and [3]) – note increased shock-standoff and reduced heat transfer rates in hypersonic flows past blunt bodies under the application of appropriate magnetic fields. The recent interest stems, however, from new revelations of a Russian concept vehicle, known as the AJAX ([4]), which made extensive reference to technologies requiring tight coupling between electromagnetic and fluid dynamic phenomena. A magnetogasdynamics (MGD) generator was proposed ([5]) to extract energy from the incoming air while simultaneously providing more benign flow to the combustion components downstream. The extracted energy could then be employed to increase thrust by MGD pumping of the flow exiting the nozzle or to assist in the generation of a plasma for injection of the body. This latter technique is known to not only reduce drag on the body but also to provide thermal protection ([6]).

In addition to daunting engineering challenges, some of the phenomena supporting the feasibility of an AJAX type vehicle are fraught with controversy (see, for example, [7]). Resolution of these issues will require extensive experimentation as well as simulation. The latter approach requires integration of several disciplines, including fluid dynamics, electromagnetics, chemical kinetics and molecular physics amongst others. This paper describes a recent effort to integrate the first two of these, within the assumptions that characterize ideal and non-ideal magnetogasdynamics.

In [8], the Euler and Navier-Stokes equations were solved, according to a finite volume formulation and symmetrical structured discretization, applied to the problem of a blunt body in two-dimensions. The work of [9] was the reference one to present the fluid dynamics and Maxwell equations of electromagnetism based on a conservative and finite volume formalisms. The [10] and the [25] symmetrical schemes were applied to solve the conserved equations. Two types of numerical dissipation models were applied, namely: [11] and [12]. A spatially variable time step

procedure was employed aiming to accelerate the convergence of the numerical schemes to the steady state solution. The results proved that, when the [10] scheme was employed, an increase in the shock standoff distance was observed, which guaranteed a minor increase in the temperature at the blunt body nose, and a minor increase in the drag aerodynamic coefficient.

In this paper, the Euler and Navier-Stokes equations are solved, according to a finite volume formulation and symmetrical unstructured discretization, applied to the problem of a blunt body in two-dimensions. The work of [9] is the reference one to present the fluid dynamics and Maxwell equations of electromagnetism based on a conservative and finite volume formalisms. The [10] symmetrical scheme is applied to solve the conserved equations. Two types of numerical dissipation models are applied, namely: [11] and [12]. A spatially variable time step procedure is employed aiming to accelerate the convergence of the numerical schemes to the steady state solution. Effective gains in terms of convergence acceleration are observed with this technique [13-14].

The results have proved that, when the [10] scheme is employed with an unstructured alternated discretization, better contours of proprieties are obtained (see [15-16]). Moreover, an increase in the shock standoff distance is observed, which guarantees a minor increase in the temperature at the blunt body nose (minor armour problems), and a minor increase in the drag aerodynamic coefficient.

2 Formulation to a Flow Submitted to a Magnetic Field

The Navier-Stokes equations to a flow submitted to a magnetic field in a perfect gas formulation are implemented on a finite volume context and two-dimensional space. The Euler equations are obtained by disregarding of the viscous vectors. These equations in integral and conservative forms can be expressed by:

$$\frac{\partial}{\partial t}\int_V Q dV + \int_S \vec{F} \bullet \vec{n} dS = 0\,, \tag{1a}$$

$$\text{with: } \vec{F} = \left(E_e - E_v\right)\vec{i} + \left(F_e - F_v\right)\vec{j}\,, \tag{1b}$$

where: Q is the vector of conserved variables, V is the computational cell volume, $\vec{F}$ is the complete flux vector, $\vec{n}$ is the unity vector normal to the flux face, S is the flux area, E_e and F_e are the convective flux vectors or the Euler flux vectors considering the contribution of the magnetic field in the x and y directions, respectively, and E_v and F_v are the viscous flux vectors considering the contribution of the magnetic field in the x and y directions, respectively. The unity vectors $\vec{i}$ and $\vec{j}$ define the system of Cartesian coordinates. The vectors Q, E_e, F_e, E_v and F_v can be defined, according to [9], as follows:

$$Q = \begin{Bmatrix} \rho \\ \rho u \\ \rho v \\ \rho Z \\ B_x \\ B_y \end{Bmatrix},\ E_e = \begin{Bmatrix} \rho u \\ \rho u^2 + P - R_b\, B_x^2/\mu_M \\ \rho uv - R_b\, B_x B_y/\mu_M \\ (\rho Z + P)u - R_b\left(\vec{V} \bullet \vec{B}/\mu_M\right)B_x \\ 0 \\ uB_y - vB_x \end{Bmatrix}, \tag{2a}$$

$$F_e = \begin{Bmatrix} \rho v \\ \rho uv - R_b\, B_x B_y/\mu_M \\ \rho v^2 + P - R_b\, B_y^2/\mu_M \\ (\rho Z + P)v - R_b\left(\vec{V} \bullet \vec{B}/\mu_M\right)B_y \\ vB_x - uB_y \\ 0 \end{Bmatrix}; \tag{2b}$$

$$E_v = \begin{Bmatrix} 0 \\ \tau_{xx}/\mathrm{Re} \\ \tau_{xy}/\mathrm{Re} \\ \left(u\tau_{xx} + v\tau_{xy}\right)/\mathrm{Re} - q_x - q_{J,x} \\ 0 \\ \dfrac{1}{\mathrm{Re}_\sigma}\dfrac{1}{\sigma}\left[\dfrac{\partial}{\partial x}\left(\dfrac{B_y}{\mu_M}\right) - \dfrac{\partial}{\partial y}\left(\dfrac{B_x}{\mu_M}\right)\right] \end{Bmatrix} \quad \text{and}$$

$$F_v = \begin{Bmatrix} 0 \\ \tau_{xy}/\mathrm{Re} \\ \tau_{yy}/\mathrm{Re} \\ \left(u\tau_{xy} + v\tau_{yy}\right)/\mathrm{Re} - q_y - q_{J,y} \\ \dfrac{1}{\mathrm{Re}_\sigma}\dfrac{1}{\sigma}\left[\dfrac{\partial}{\partial y}\left(\dfrac{B_x}{\mu_M}\right) - \dfrac{\partial}{\partial x}\left(\dfrac{B_y}{\mu_M}\right)\right] \\ 0 \end{Bmatrix}, \tag{3}$$

in which: ρ is the fluid density; u and v are the Cartesian components of the velocity vector in the x and y directions, respectively; Z is the flow total energy considering the contribution of the magnetic field; B_x and B_y are the Cartesian components of the magnetic field vector active in the x and y directions, respectively; P is the pressure term considering the magnetic field effect; R_b is the magnetic force number or the pressure number; μ_M is the mean

magnetic permeability, with the value $4\pi x10^{-7}$ T.m/A to the atmospheric air; $\vec{V}$ is the flow velocity vector in Cartesian coordinates; $\vec{B}$ is the magnetic field vector in Cartesian coordinates; the τ's are the components of the viscous stress tensor defined at the Cartesian plane; q_x and q_y are the components of the Fourier heat flux vector in the x and y directions, respectively; $q_{J,x}$ and $q_{J,y}$ are the components of the Joule heat flux vector in the x and y directions, respectively; Re_σ is the magnetic Reynolds number; and σ is the electrical conductivity.

The viscous stresses, in N/m^2, are determined, according to a Newtonian fluid model, by:

$$\tau_{xx} = 2\mu\frac{\partial u}{\partial x} - \frac{2}{3}\mu\left(\frac{\partial u}{\partial x} + \frac{\partial v}{\partial y}\right), \tau_{xy} = \mu\left(\frac{\partial u}{\partial y} + \frac{\partial v}{\partial x}\right), \quad (4a)$$

$$\tau_{yy} = 2\mu\frac{\partial v}{\partial y} - \frac{2}{3}\mu\left(\frac{\partial u}{\partial x} + \frac{\partial v}{\partial y}\right), \quad (4b)$$

where μ is the fluid molecular viscosity. In this work, the empiric formula of Sutherland was employed to the calculation of the molecular viscosity (details in [17]).

Z is the total energy defined by:

$$Z = \frac{p}{(\gamma-1)\rho} + \frac{u^2+v^2}{2} + R_b\frac{B^2}{2\mu_M\rho} = \frac{p}{(\gamma-1)\rho} + \frac{u^2+v^2}{2} + R_b\frac{\left(B_x^2+B_y^2\right)}{2\mu_M\rho}. \quad (5)$$

The pressure term is expressed by:

$$P = p + R_b\frac{B^2}{2\mu_M} = p + R_b\frac{\left(B_x^2+B_y^2\right)}{2\mu_M}. \quad (6)$$

The magnetic force number or pressure number is determined by:

$$R_b = \frac{B_\infty^2}{\rho_\infty V_\infty^2\mu_{M,\infty}} = \frac{\left(B_{x,\infty}^2+B_{y,\infty}^2\right)}{\rho_\infty\left(u_\infty^2+v_\infty^2\right)\mu_{M,\infty}}. \quad (7)$$

The laminar Reynolds number is defined by:

$$\mathrm{Re} = \frac{\rho_\infty V_\infty L}{\mu_\infty}, \quad (8)$$

in which "∞" represents freestream properties, V_∞ represents the characteristic flow velocity and L is a characteristic length of the studied configuration.

The magnetic Reynolds number is calculated by:

$$\mathrm{Re}_\sigma = LV_\infty\mu_{M,\infty}\sigma_\infty. \quad (9)$$

The components of the Fourier heat flux vector are expressed by:

$$q_x = -\frac{\mu}{(\gamma-1)\mathrm{Pr}\,M_\infty^2\,\mathrm{Re}}\frac{\partial T}{\partial x} \quad \text{and}$$

$$q_y = -\frac{\mu}{(\gamma-1)\mathrm{Pr}\,M_\infty^2\,\mathrm{Re}}\frac{\partial T}{\partial y}, \quad (10)$$

with:

$\mathrm{Pr} = \mu_\infty Cp/k$ = 0.72, is the laminar Prandtl number; (11)

$M_\infty = \frac{V_\infty}{\sqrt{\gamma p/\rho}}$, is the freestream Mach number; (12)

γ is the ratio of specific heats to a perfect gas, with a value of 1.4 to atmospheric air.

The components of the Joule heat flux vector, which characterizes the non-ideal formulation, are determined by:

$$q_{J,x} = -\frac{R_b}{R_\sigma}\left\{\frac{B_y}{\mu_M\sigma}\left[\frac{\partial}{\partial x}\left(\frac{B_y}{\mu_M}\right) - \frac{\partial}{\partial y}\left(\frac{B_x}{\mu_M}\right)\right]\right\} \quad \text{and}$$

$$q_{J,y} = -\frac{R_b}{R_\sigma}\left\{\frac{B_x}{\mu_M\sigma}\left[\frac{\partial}{\partial y}\left(\frac{B_x}{\mu_M}\right) - \frac{\partial}{\partial x}\left(\frac{B_y}{\mu_M}\right)\right]\right\}. \quad (13)$$

3 Jameson and Mavriplis Unstructured Algorithm in 2D

First of all, the system geometrical parameters are defined. Afterwards, the numerical scheme will be described. The cell volume on an unstructured context is defined by:

$$V_i = 0.5\left|\left(x_{n1}y_{n2} + y_{n1}x_{n3} + x_{n2}y_{n3}\right) - \left(x_{n3}y_{n2} + y_{n3}x_{n1} + x_{n2}y_{n1}\right)\right|, \quad (14)$$

with n_1, n_2 and n_3 being the nodes of a given triangular cell. The description of the computational

cell and its nodes, flux interfaces and neighbours are shown in Fig. 1.

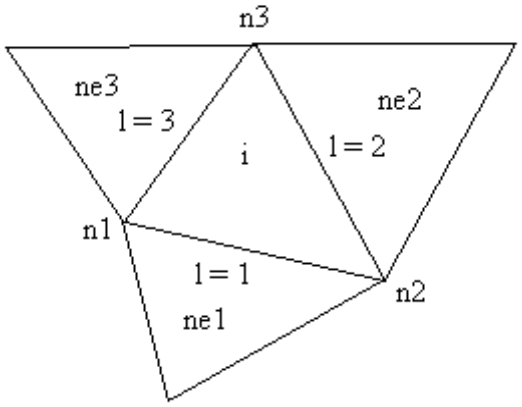

Figure 1 : Schematic of a cell and its neighbours, nodes and flux interfaces.

The area components at the "l" interface are defined by:

$$S_x^l = n_x^l S^l \quad \text{and} \quad S_y^l = n_y^l S^l, \tag{15}$$

where n_x^l, n_y^l and S^l are defined as:

$$n_x^l = \Delta y_l \Big/ \left(\Delta x_l^2 + \Delta y_l^2\right)^{0.5},\ n_y^l = -\Delta x_l \Big/ \left(\Delta x_l^2 + \Delta y_l^2\right)^{0.5};$$
$$S^l = \left(\Delta x_l^2 + \Delta y_l^2\right)^{0.5}. \tag{16}$$

Expressions to Δx_l and Δy_l are given in Tab. 1.

Table 1. Values of Δx_l and Δy_l.

Interface	Δx_l	Δy_l
l = 1	$x_{n2} - x_{n1}$	$y_{n2} - y_{n1}$
l = 2	$x_{n3} - x_{n2}$	$y_{n3} - y_{n2}$
l = 3	$x_{n1} - x_{n3}$	$y_{n1} - y_{n3}$

Now, Equation (1) can be rewritten following an unstructured spatial discretization context ([18] and [10]) as:

$$d\left(V_i Q_i\right)/dt + C(Q_i) = 0, \tag{17}$$

where:

$$C(Q_i) = \left\{0.5\left[\left(E_e\right)_i + \left(E_e\right)_{ne1}\right] - \left(E_v\right)_{l=1}\right\} S_{x_{l=1}} +$$
$$\left\{0.5\left[\left(F_e\right)_i + \left(F_e\right)_{ne1}\right] - \left(F_v\right)_{l=1}\right\} S_{y_{l=1}} +$$
$$\left\{0.5\left[\left(E_e\right)_i + \left(E_e\right)_{ne2}\right] - \left(E_v\right)_{l=2}\right\} S_{x_{l=2}} + \tag{18a}$$
$$\left\{0.5\left[\left(F_e\right)_i + \left(F_e\right)_{ne2}\right] - \left(F_v\right)_{l=2}\right\} S_{y_{l=2}} +$$
$$\left\{0.5\left[\left(E_e\right)_i + \left(E_e\right)_{ne3}\right] - \left(E_v\right)_{l=3}\right\} S_{x_{l=3}} +$$
$$\left\{0.5\left[\left(F_e\right)_i + \left(F_e\right)_{ne3}\right] - \left(F_v\right)_{l=3}\right\} S_{y_{l=3}}. \tag{18b}$$

is the approximation to the flux integral of Eq. (1). In this work, one adopts that, for example, the flux vector E_e at the flux interface l = 1 is obtained by the arithmetical average between the E_e vector calculated at the cell "i" and the E_e vector calculated at its neighbor ne1. The viscous flux vectors are calculated in a symmetrical form as demonstrated in section **4**.

The spatial discretization proposed by the authors is equivalent to a symmetrical scheme with second order accuracy, on a finite difference context. The introduction of an artificial dissipation operator "D" is necessary to guarantee the scheme numerical stability in presence of, for example, uncoupled odd/even solutions and non-linear stabilities, as shock waves. Equation (17) can, so, be rewritten as:

$$d\left(V_i Q_i\right)/dt + \left[C(Q_i) - D(Q_i)\right] = 0. \tag{19}$$

The time integration is performed by a hybrid Runge-Kutta method of five stages, with second order accuracy, and can be represented in general form as:

$$Q_i^{(0)} = Q_i^{(n)}$$
$$Q_i^{(k)} = Q_i^{(0)} - \alpha_k\, \Delta t_i \Big/ V_i \left[C\left(Q_i^{(k-1)}\right) - D\left(Q_i^{(m)}\right)\right], \tag{20}$$
$$Q_i^{(n+1)} = Q_i^{(k)}$$

where: k = 1,...,5; m = 0 until 4; $\alpha_1 = 1/4$, $\alpha_2 = 1/6$, $\alpha_3 = 3/8$, $\alpha_4 = 1/2$ and $\alpha_5 = 1$. [10] suggest that the artificial dissipation operator should be evaluated only in the first two stages as the Euler equations were solved (m = 0, k = 1 and m = 1, k = 2). [19] suggest that the artificial dissipation operator should be evaluated in alternated stages as the Navier-Stokes equations were solved (m = 0, k = 1, m = 2, k = 3 and m = 4, k = 5). These procedures aim CPU time economy and also better damping of the numerical instabilities originated from the discretization based on the hyperbolic characteristics of the Euler equations and the hyperbolic/parabolic characteristics of the Navier-Stokes equations.

3.1 Artificial dissipation operator

The artificial dissipation operator implemented in the [10] schemes has the following structure, based on the works of [20-21]:

$$D(Q_i) = d^{(2)}(Q_i) - d^{(4)}(Q_i), \quad (21)$$

where:

$$d^{(2)}(Q_i) = 0.5\varepsilon^{(2)}_{l=1}(A_i + A_{ne1})(Q_{ne1} - Q_i) + 0.5\varepsilon^{(2)}_{l=2}(A_i + A_{ne2})(Q_{ne2} - Q_i) + 0.5\varepsilon^{(2)}_{l=3}(A_i + A_{ne3})(Q_{ne3} - Q_i), \quad (22)$$

named undivided Laplacian operator, is responsible by the numerical stability in the presence of shock waves; and

$$d^{(4)}(Q_i) = 0.5\varepsilon^{(4)}_{l=1}(A_i + A_{ne1})(\nabla^2 Q_{ne1} - \nabla^2 Q_i) + 0.5\varepsilon^{(4)}_{l=2}(A_i + A_{ne2j})(\nabla^2 Q_{ne2} - \nabla^2 Q_i) + 0.5\varepsilon^{(4)}_{l=3}(A_i + A_{ne3})(\nabla^2 Q_{ne3} - \nabla^2 Q_i), \quad (23)$$

named bi-harmonic operator, is responsible by the background stability (for example: instabilities originated from uncoupled odd/even solutions). In this last term,

$$\nabla^2 Q_i = (Q_{ne1} - Q_i) + (Q_{ne2} - Q_i) + (Q_{ne3} - Q_i). \quad (24)$$

In the $d^{(4)}$ operator, $\nabla^2 Q_i$ is extrapolated from the value of the real neighbor cell every time that it represent a ghost cell. The ε terms are defined, for example, as:

$$\varepsilon^{(2)}_{l=1} = K^{(2)} MAX\ (\nu_i, \nu_{ne1}) \text{ and}$$
$$\varepsilon^{(4)}_{l=1} = MAX\ [0, (K^{(4)} - \varepsilon^{(2)}_{l=1})], \quad (25)$$

with:

$$\nu_i = \left(|p_{ne1} - p_i| + |p_{ne2} - p_i| + |p_{ne3} - p_i|\right) / (p_{ne1} + p_{ne2} + p_{ne3} + 3p_i) \quad (26)$$

representing a pressure sensor employed to identify regions of elevated gradients. The $K^{(2)}$ and $K^{(4)}$ constants has typical values of 1/4 and 3/256, respectively. Every time that a neighbor cell represents a ghost cell, one assumes, for example, that $\nu_{ghost} = \nu_i$.

The A_i terms can be defined according to two models implemented in this work: (a) [11] and (b) [12]. In the first case, the A_i terms are contributions from the maximum normal eigenvalue of the Euler equations integrated along each cell face. Hence, they are defined as follows:

(a) [11] model:

$$A_i = \left[\left|0.5(u_i + u_{ne1})S_{x_{l=1}} + 0.5(v_i + v_{ne1})S_{y_{l=1}}\right|\right] + 0.5(a_i + a_{ne1})\left(S^2_{x_{l=1}} + S^2_{y_{l=1}}\right)^{0.5} + \left[\left|0.5(u_i + u_{ne2})S_{x_{l=2}} + 0.5(v_i + v_{ne2})S_{y_{l=2}}\right|\right] + 0.5(a_i + a_{ne2})\left(S^2_{x_{l=2}} + S^2_{y_{l=2}}\right)^{0.5} + \left[\left|0.5(u_i + u_{ne3})S_{x_{l=3}} + 0.5(v_i + v_{ne3})S_{y_{l=3}}\right|\right] + 0.5(a_i + a_{ne3})\left(S^2_{x_{l=3}} + S^2_{y_{l=3}}\right)^{0.5}, \quad (27)$$

where "*a*" represents the sound speed.

(b) [12] model:

$$A_i = V_i / \Delta t_i\ , \quad (28)$$

which represents a scaling factor, according to structured meshes, with the desired behavior to the artificial dissipation term: (i) bigger control volumes result in bigger value to the dissipation term; (ii) smaller time steps also result in bigger values to the scaling term.

4 Calculations of the Viscous Gradients

The viscous vectors at the flux interface are obtained by the arithmetical average between the primitive variables at the right and left states of the flux interface, as also the arithmetical average of the primitive variable gradients, also considering the right and left states of the flux interface. The gradients of the primitive variables present in the viscous flux vectors are calculated employing the Green theorem, which considers that the gradient of a primitive variable is constant in the volume and that the volume integral which defines this gradient is replaced by a surface integral. This methodology to calculation of the viscous gradients is based on the work of [22]. As an example, one has to $\partial u/\partial x$:

$$\frac{\partial u}{\partial x} = \frac{1}{V}\int_V \frac{\partial u}{\partial x} dV = \frac{1}{V}\int_S u(\vec{n} \bullet d\vec{S}) = \frac{1}{V}\int_{S_x} u dS_x \cong \frac{1}{V_{i,j}}\left[0.5(u_i + u_{ne1})S_{x_{l=1}} + 0.5(u_i + u_{ne2})S_{x_{l=2}} + 0.5(u_i + u_{ne3})S_{x_{l=3}}\right]. \quad (29)$$

5 Dimensionless, Initial and Boundary Conditions, Computational Domain and Employed Meshes

5.1 Dimensionless

The dimensionless employed to the case of the flowfield submitted to a magnetic field in two-dimensions are detailed as follows: ρ is dimensionless in relation to ρ_∞; the u and v Cartesian components of velocity are dimensionless in relation to the freestream speed of sound, a_∞; p is dimensionless in relation to the product between ρ_∞ and the squared of a_∞; the translational/rotational temperature is dimensionless in relation to a_∞; the molecular viscosity is dimensionless in relation to μ_∞; the Cartesian components of the induced magnetic field is dimensionless by B_∞; the magnetic permeability of the mean is dimensionless by $\mu_{M,\infty}$; and the electric conductivity is dimensionless by σ_∞.

5.2 Initial and boundary conditions

5.2.1 Initial condition

The initial condition adopts freestream flow properties to the conserved variables. Due to the present dimensionless, the vector of conserved variables in the field is determined as follows:

$$Q = \begin{Bmatrix} 1.0 \\ M_\infty \cos\theta \\ M_\infty \sin\theta \\ \dfrac{1}{\gamma(\gamma-1)} + 0.5M_\infty^2 + 0.5R_b \\ B_{x,\infty} / B_\infty \\ B_{y,\infty} / B_\infty \end{Bmatrix}, \qquad (30)$$

where θ is the angle of attack, M_∞ is the freestream Mach number, $B_{x,\infty}$, $B_{y,\infty}$, B_∞ are the Cartesian components of the induced magnetic field and the modulus of the induced magnetic field, and R_b is calculated according to Eq. (7).

5.2.2 Boundary conditions

The boundary conditions are basically of three types: solid wall, entrance and exit. These conditions are implemented in special cells named "ghost cells".

(a) Solid wall condition: In the inviscid case, this condition imposes the flow tangency at wall. This condition is satisfied considering the velocity component tangent to the wall relative to the ghost cell as equal to the respective component of the real neighbor cell. At the same time, the velocity component normal to the wall relative to the ghost cell is equaled to the negative of the respective component of the real neighbor cell. This procedure leads to a system of equations which results to:

$$u_g = \left(n_y^2 - n_x^2\right)u_r + \left(-2n_x n_y\right)v_r \quad \text{and}$$
$$v_g = \left(-2n_x n_y\right)u_r + \left(n_x^2 - n_y^2\right)v_r, \qquad (31)$$

where "g" indicate ghost cell properties and "r" indicate real cell properties. In the viscous case, the Cartesian components of the velocity vector of the ghost cells are equaled in value, but with the opposed signal, with the respective Cartesian components of the real cell.

$$u_g = -u_r \quad \text{and} \quad v_g = -v_r. \qquad (32)$$

In both cases, inviscid and viscous, the pressure gradient normal to the wall is equaled to zero, according to an inviscid formulation in the former case and to the boundary layer condition in the latter. The same hypothesis is employed to the temperature gradient normal to the wall, considering an adiabatic wall. With these conditions, ghost cell density and pressure are extrapolated from the respective values of the real neighbor cell (zero order extrapolation).

The Cartesian components of the induced magnetic field at the wall to the ghost cells are fixed with their initial values. The magnetic permeability is considered constant with its initial value. The total energy Z to the ghost cell is calculated by:

$$Z_g = \frac{p_g}{(\gamma-1)\rho_g} + 0.5\left(u_g^2 + v_g^2\right) + 0.5R_b \frac{B_{x,g}^2 + B_{y,g}^2}{\mu_{M,g}\rho_g}. \qquad (33)$$

(b) Entrance condition:

(b.1) Subsonic flow: Five properties are specified and one is extrapolated, based on the analysis of information propagation along the characteristic directions in the calculation domain ([23]). In other words, five characteristic directions of information propagation points to inside the computational domain and should be specified, to the subsonic flow. Only the characteristic direction associated with the "$(q_n$-a)" eigenvalue cannot be specified and should be determined by interior information of the calculation domain. The pressure is the extrapolated variable from the real neighbor cell. Density, Cartesian velocity components and Cartesian induced magnetic field components have their values determined by the initial condition. The total energy is determined by Eq. (33).

(b.2) Supersonic flow: All variables are fixed with their initial values.

(c) Exit condition:

(c.1) Subsonic flow: Five characteristic directions of information propagation points outward from the computational domain and should be extrapolated from the interior information. The characteristic direction associated with the eigenvalue "(q_n-a)" should be specified because points inward the calculation domain ([23]). In this case, the ghost cell pressure is specified by its initial value. Density, Cartesian velocity components and Cartesian induced magnetic field components are extrapolated and the total energy is determined by Eq. (33).
(c.2) Supersonic flow: All variables are extrapolated from the interior domain due to the fact that all six characteristic directions of information propagation of the Euler equations point outward from the calculation domain and, with it, nothing can be fixed.

5.3 Computational domain

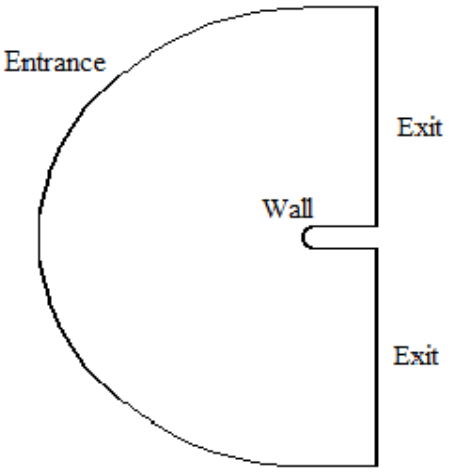

Figure 2 : Blunt body computational domain.

Figure 2 presents the geometry and the computational domain employed in the unstructured simulations in two-dimensions. This figure describes a blunt body with nose ratio of 1.0m and the far field located at twenty times the nose ratio in relation to the configuration nose. The domain presents three frontiers, as related in the boundary conditions, namely: solid wall, entrance and exit.

5.4 Employed meshes

Figures 3 and 4 present the meshes employed to the inviscid unstructured simulations in two-dimensions for the case of a flow submitted to an induced magnetic field around a blunt body. Two cases are distinguished: SS – Same Sense, and AS – Alternated Sense.

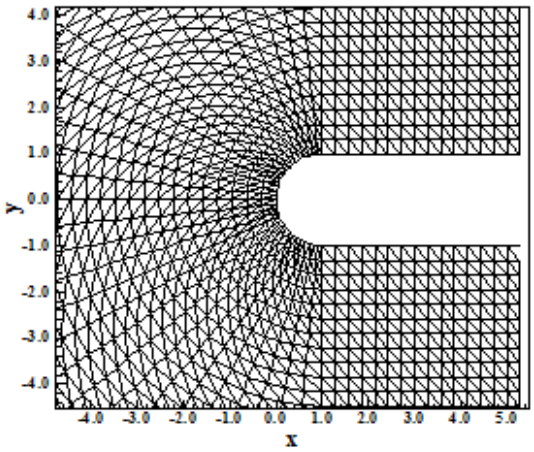

Figure 3 : Unstructured mesh to the inviscid 2D case (SS).

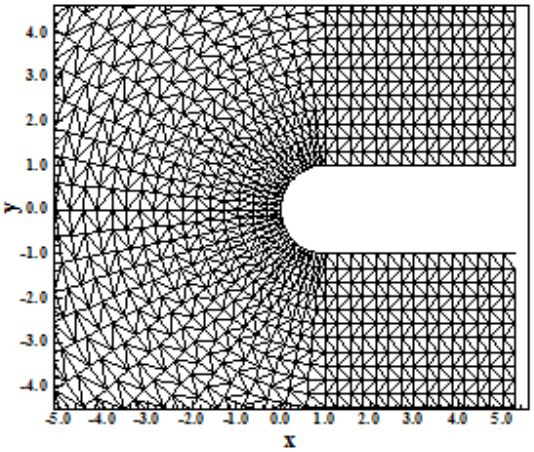

Figure 4 : Unstructured mesh to the inviscid 2D case (AS).

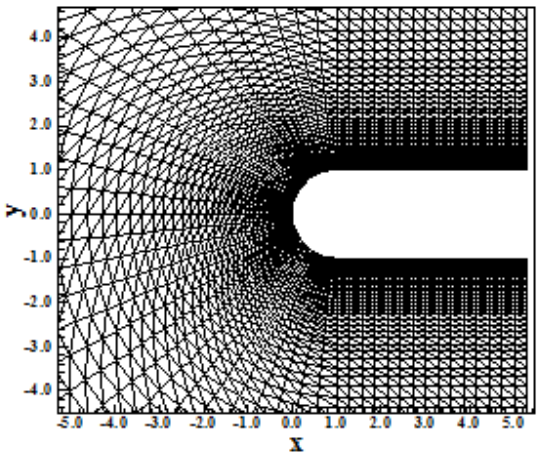

Figure 5 : Unstructured mesh to the viscous 2D case (SS).

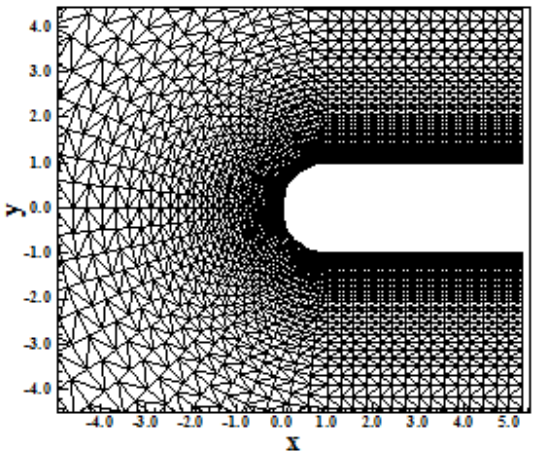

Figure 6 : Unstructured mesh to the viscous 2D case (AS).

Figure 5 and 6 exhibits the meshes used to the viscous simulations. The mesh to the viscous case presents an exponential stretching in the η direction of 7.5%. The mesh to the inviscid case is composed of 7,440 triangular cells and 3,843 nodes, which corresponds to a finite difference mesh of 63x61 points. The mesh to the viscous case is composed by the same number of cells and nodes, also corresponding to a mesh of 63x61 points.

6 Results

Tests were performed in a notebook with processor INTEL PENTIUM Dual Core of 2.3GHz of clock and 2.0GBytes of RAM. As the interest of this work is steady state problems, one needs to define a criterion which guarantees that such condition was reached. The criterion adopted in this work was to consider a reduction of no minimal three (3) orders in the magnitude of the maximum residual in the domain, a typical criterion in the CFD community. The residual to each cell was defined as the numerical value obtained from the discretized conservation equations. As there are six (6) conservation equations to each cell, the maximum value obtained from these equations is defined as the residual of this cell. Thus, this residual is compared with the residual of the other cells, calculated of the same way, to define the maximum residual in the domain. In the simulations, the attack angle, α, was set equal to zero.

6.1 Initial conditions

The initial conditions to the standard simulation of the studied algorithm are presented in Tab. 2. This is a standard case to the ideal gas flow submitted to a magnetic field normal to the symmetry line of the configuration under study. The Reynolds number was calculated from the data of [24].

Table 2 : Initial conditions of the simulations in 2D.

Property	Value
M_∞	10.6
$B_{y,\infty}$	0.15 T
μ_M	1.2566×10^{-6} T.m/A
σ_∞	1,000 ohm/m
Altitude	40,000 m
Pr	0.72
L (2D)	2.0 m
Re_∞ (2D)	1.6806×10^6

6.2. Results to inviscid flow in 2D – Mavriplis operator

Figures 7 and 8 present the pressure contours calculated at the computational domain to the ideal gas flow, inviscid, submitted to a magnetic field.

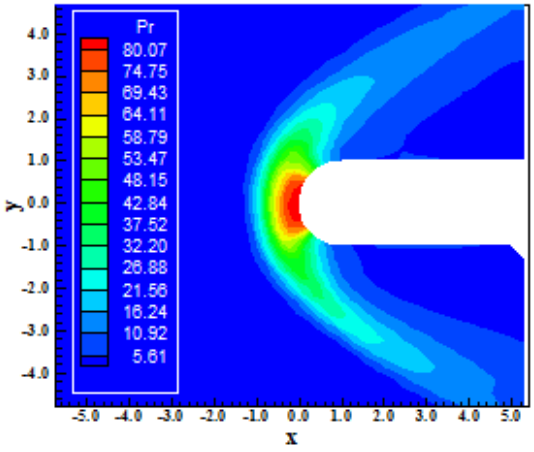

Figure 7 : Pressure contours (Mav/SS).

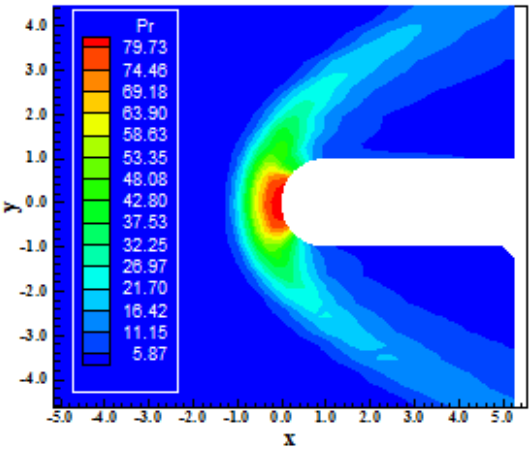

Figure 8 : Pressure contours (Mav/AS).

As can be observed, the pressure field generated by [10] using the [11] artificial dissipation operator is more severe than that obtained with [12]. Moreover, the unstructured alternated discretization provides a more symmetrical pressure field than the same sense discretrization.

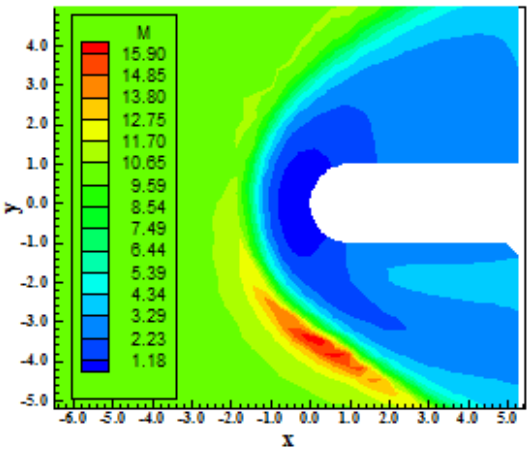

Figure 9 : Mach number contours (Mav/SS).

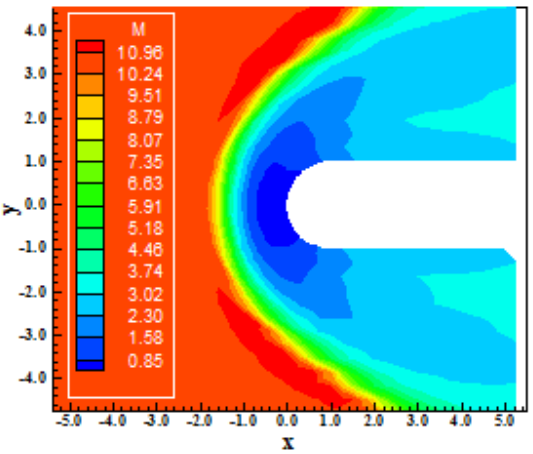

Figure 10 : Mach number contours (Mav/AS).

Figures 9 and 10 show the Mach number contours calculated at the computational domain by the [10] scheme employing the artificial dissipation models of [11] and [12], respectively. The Mach number field obtained by the [10] scheme generated at the AS condition is better predicted than as using the SS condition. Moreover, Fig. 9 presents a strength pre-shock oscillation, which is traduced by an asymmetrical solution. Good symmetry properties are observed in the 10 solution. The shock wave develops naturally, passing from a normal shock at the symmetry line to oblique shock waves along the body and finishing in a Mach wave, far from the geometry.

Figures 11 and 12 present the translational / rotational temperature distributions calculated at the computational domain. The [10] scheme with the alternated spatial discretization, AS, predicts a more symmetrical temperature field. However, the SS solution presents a more severe temperature peak.

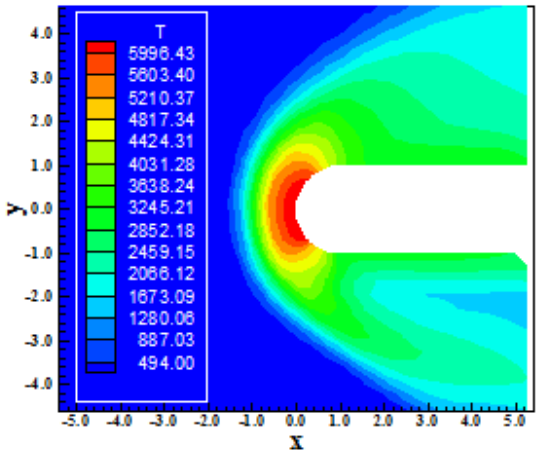

Figure 11 : Temperature contours (Mav/SS).

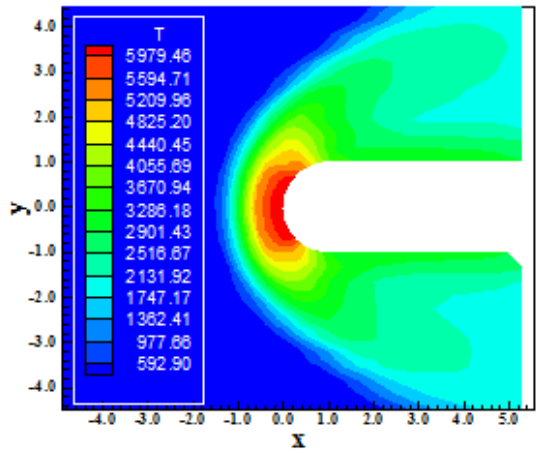

Figure 12 : Temperature contours (Mav/AS).

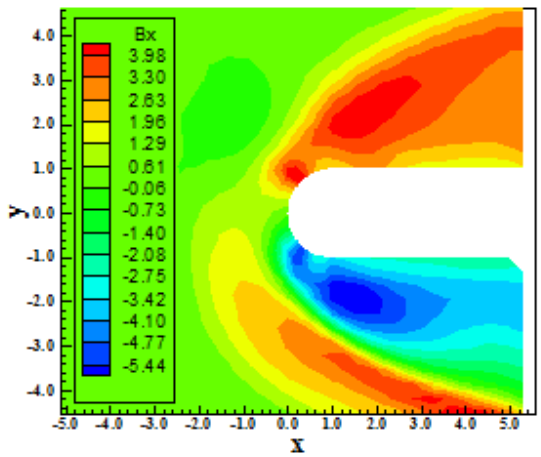

Figure 13 : B_x component of magnetic field (Mav/SS).

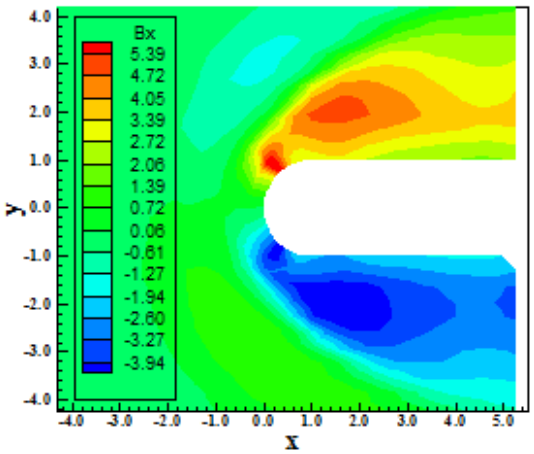

Figure 14 : B_x component of magnetic field (Mav/AS).

Figures 13 and 14 exhibit the contours of the B_x component of the magnetic field vector determined at the calculation domain. As can be observed, the B_x component is negative at the geometry lower surface and positive at the geometry upper surface, indicating that the magnetic field performs a curve around the geometry. The solution presented by the [10] scheme with the AS discretization is quantitatively more symmetrical than the respective one obtained with the SS discretization.

Figures 15 and 16 exhibit the magnetic vector field with induction lines to highlight the satisfied initial condition far ahead of the configuration and the distortion in these lines close to the blunt body. As can be observed, the magnetic induction lines are initially attracted to the magnetic field imposed at the blunt body walls and, close to the body, suffer distortion, getting round the configuration. It can be also observed that the solution with AS discretization is better defined than with SS discretization, ratifying the behavior observed in [15-16].

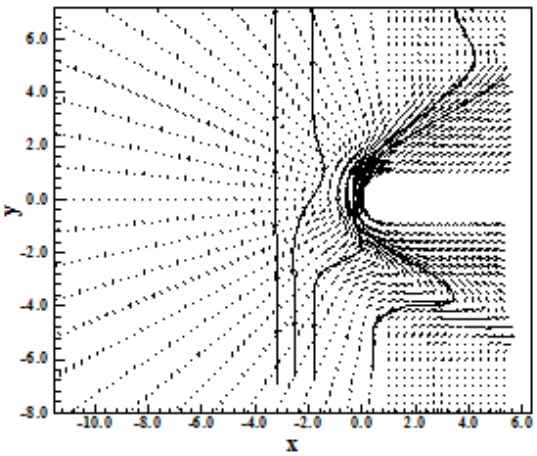

Figure 15 : Magnetic field and induction lines (Mav/SS).

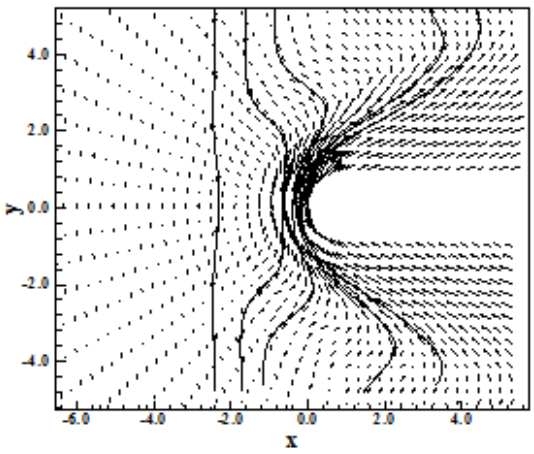

Figure 16 : Magnetic field and induction lines (Mav/AS).

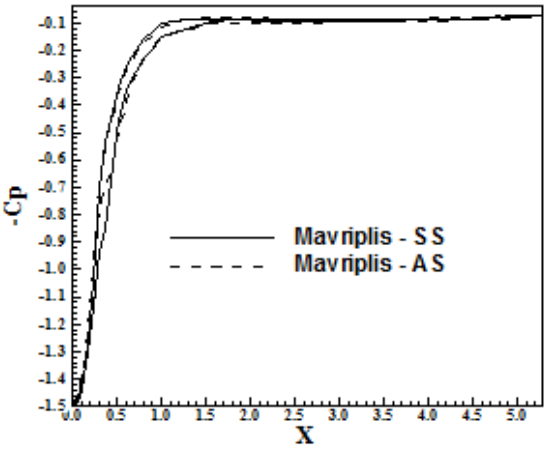

Figure 17 : -Cp distributions.

Figure 17 shows the –Cp distributions along the blunt body wall, due to the SS and AS discretization as using the [11] operator. As can be seen, the shock captured by the [10] scheme does not present any significant differences as using SS or AS discretizations.

6.3. Results to inviscid flow in 2D – Azevedo operator

Figures 18 and 19 exhibit the pressure contours calculated at the computational domain. The pressure field obtained by the [10] scheme employing the AS spatial discretization is more symmetrical than that obtained with the SS discretization. However, the former presents a more intense pressure peak than that obtained with the later.

Figures 20 and 21 present the Mach number field generated by the [10] scheme, in SS and AS spatial discretizations. Again is observed a pre-shock oscillation in front of the blunt body, which

damages the severely solution. The most symmetrical Mach number field is obtained with the AS discretization.

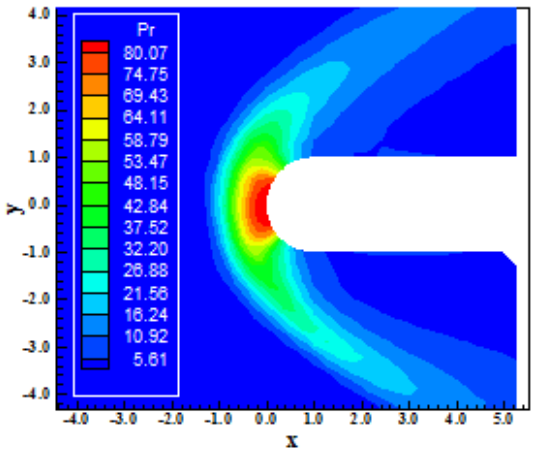

Figure 18 : Pressure contours (Az/SS).

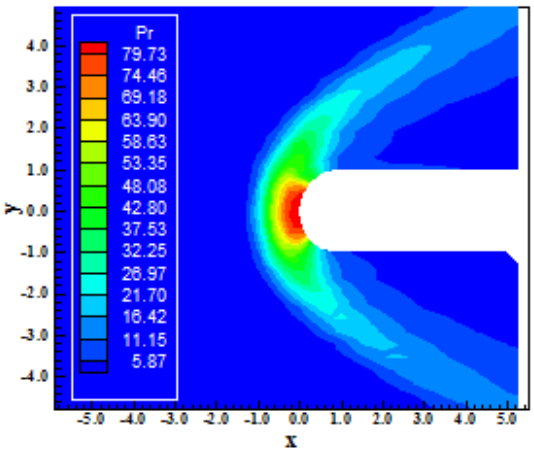

Figure 19 : Pressure contours (Az/AS).

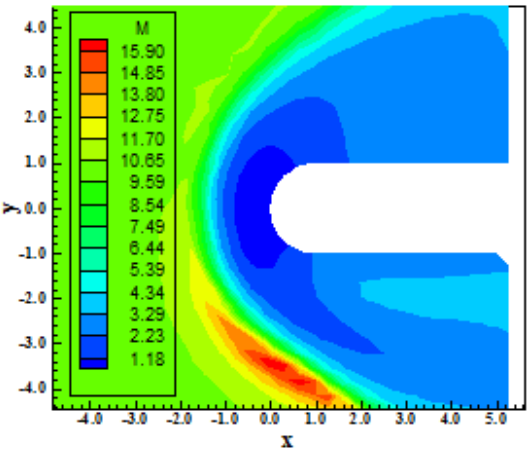

Figure 20 : Mach number contours (Az/SS).

It is important to note that both solutions present pre-shock oscillation problems, being more critical those observed in the solution with SS discretization. Good symmetry properties are observed in the AS solution.

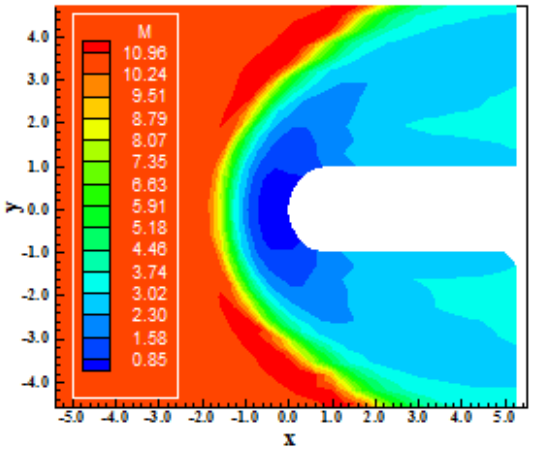

Figure 21 : Mach number contours (Az/AS).

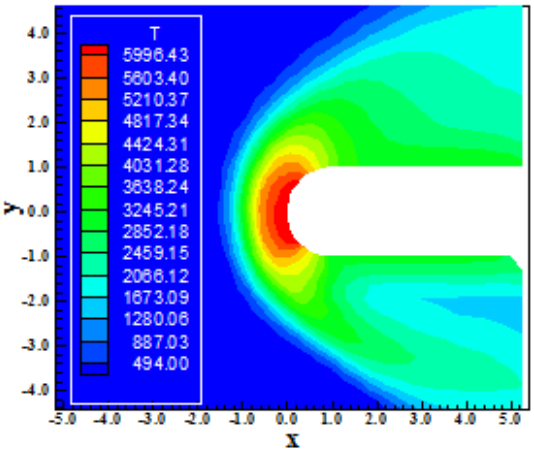

Figure 22 : Temperature contours (Az/SS).

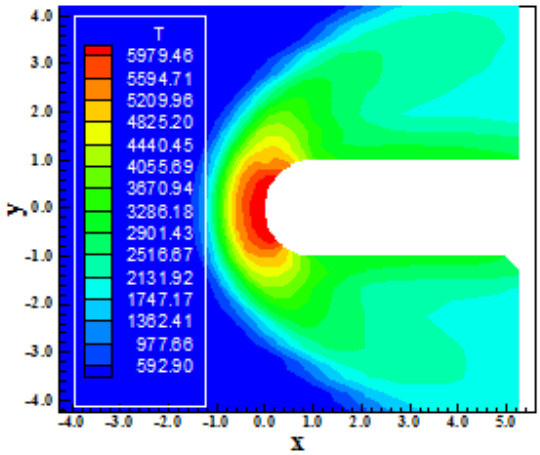

Figure 23 : Temperature contours (Az/AS).

Figures 22 and 23 present the translational / rotational temperature distributions calculated at the computational domain. The [10] scheme with the

AS spatial discretization presents a more symmetrical solution. The [12] artificial dissipation model predicts a more severe temperature field in the SS case.

Figures 24 and 25 exhibit the contours of the B_x component of the magnetic field vector determined at the calculation domain. As can be observed, the B_x component is negative at the geometry lower surface and positive at the geometry upper surface, indicating that the magnetic field performs a curve around the geometry. The solutions presented by the [10] scheme with the AS spatial discretization is more symmetrical than the SS discretization.

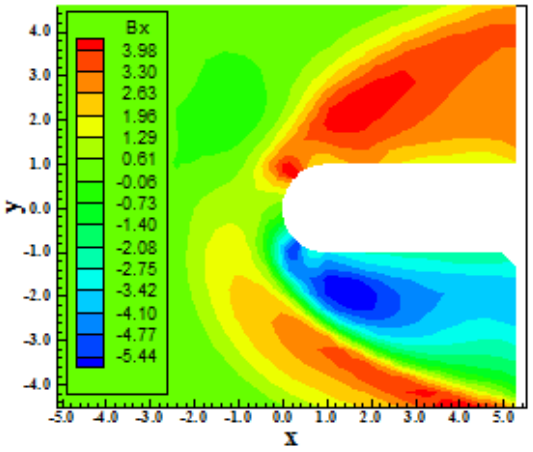

Figure 24 : B_x component of magnetic field (Az/SS).

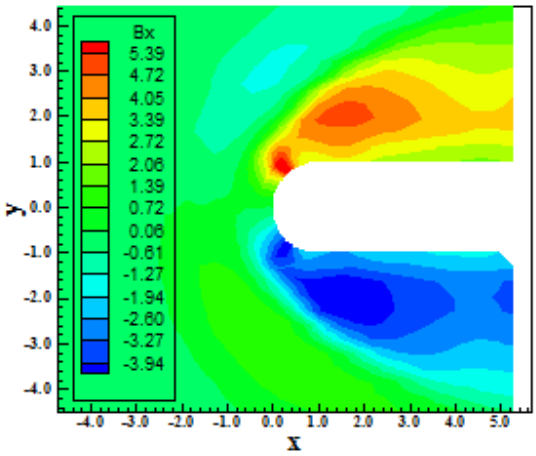

Figure 25 : B_x component of magnetic field (Az/AS).

Figures 26 and 27 exhibit the magnetic vector field with induction lines to highlight the satisfied initial condition far ahead of the configuration and the distortion in these lines close to the blunt body. As can be observed, the magnetic induction lines are initially attracted to the magnetic field imposed at the blunt body walls and, close to the body, suffer distortion, getting round the configuration. The AS spatial discretization is more symmetrical than the SS spatial discretization.

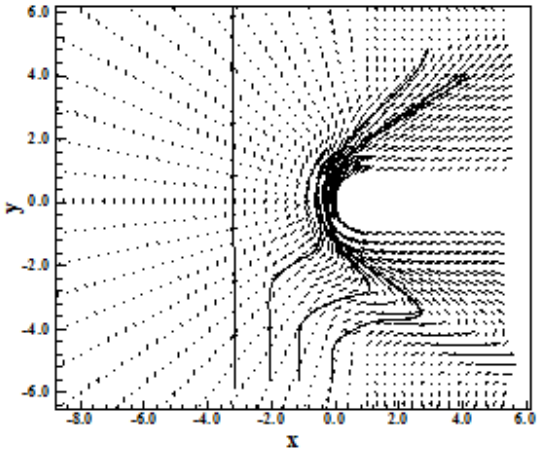

Figure 26 : Magnetic field and induction lines (Az/SS).

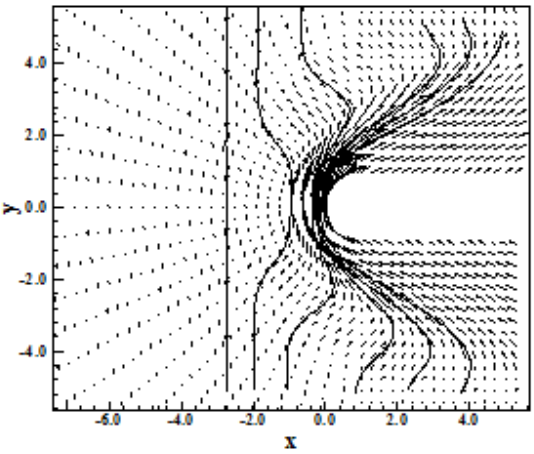

Figura 27 : Magnetic field and induction lines (Az/AS).

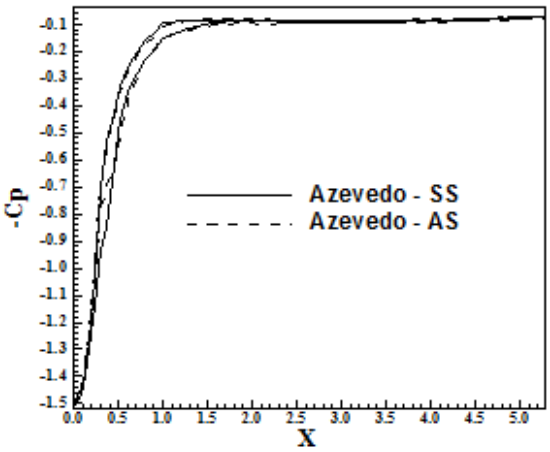

Figure 28 : -Cp distributions.

Figure 28 shows the –Cp distributions along the blunt body wall. As can be seen, the shock captured by the [10] scheme practically does not present any

differences in the SS and AS cases. Moreover, both –Cp profiles are very smooth, without pre-shock oscillations.

6.4. Results to viscous flow in 2D – Mavriplis operator

Figure 29 and 30 present the pressure contours calculated at the computational domain. The pressure contours obtained by the [10] scheme calculated at the AS discretization is more symmetrical than that obtained with the SS discretization. Good symmetry properties are observed in the AS solution.

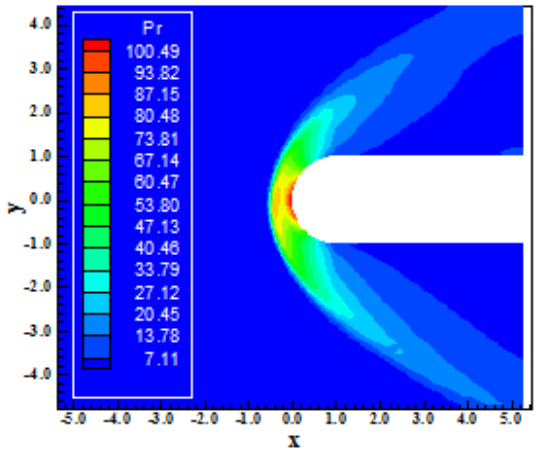

Figure 29 : Pressure contours (Mav/SS).

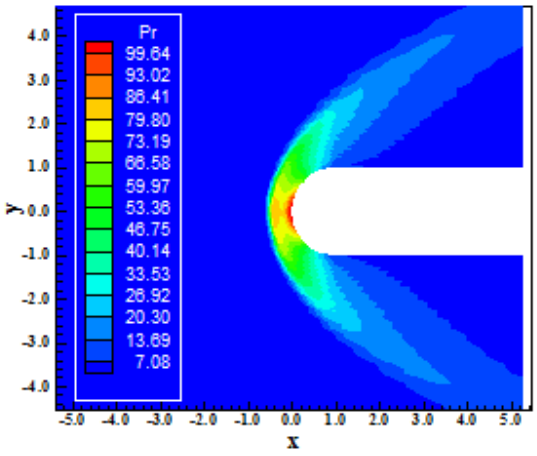

Figure 30 : Pressure contours (Mav/AS).

Figures 31 and 32 exhibit the Mach number contours calculated at the computational domain by the [10] scheme employing the artificial dissipation model of [11]. The Mach number field obtained by the [10] scheme calculated at the AS discretization presents better symmetry properties than the SS discretization. The shock wave develops naturally, passing from a normal shock (frontal) to a Mach wave, through oblique shock waves. Both solutions present pre-shock oscillations, being in the AS case a more symmetrical distribution of the Mach number contours.

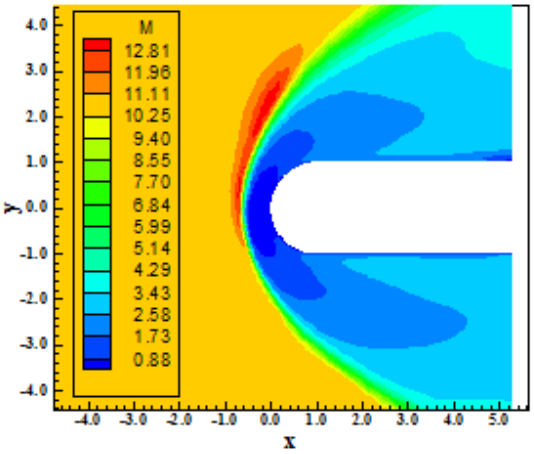

Figure 31 : Mach number contours (Mav/SS).

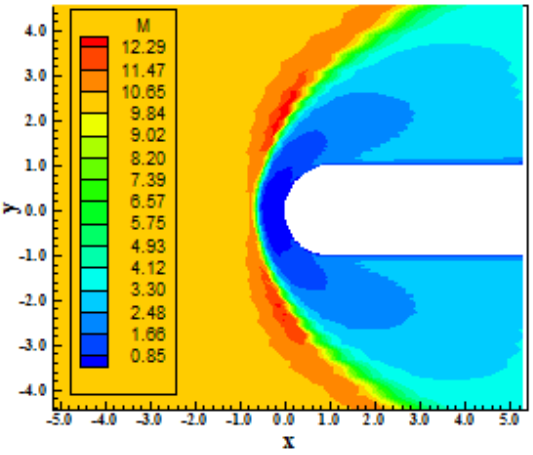

Figure 32 : Mach number contours (Mav/AS).

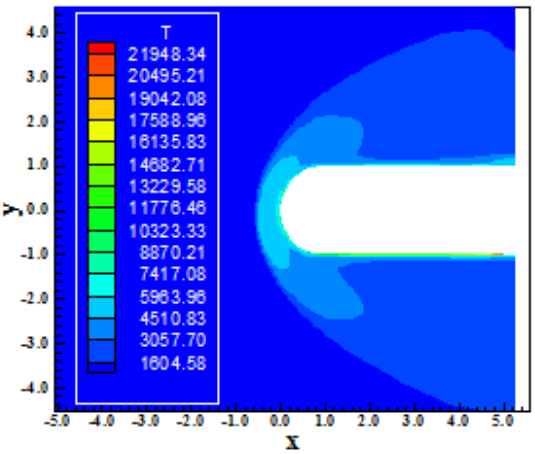

Figure 33 : Temperature contours (Mav/SS).

Figures 33 and 34 show the translational / rotational temperature distributions calculated at the computational domain. The [10] scheme solution obtained at the AS spatial discretization presents more symmetrical behavior. A significant difference between temperature fields is notable. The temperature peak at the SS case is near 22,000 K, whereas at the AS case is about 13,000 K. This difference could be due to the artificial dissipation model or due to the spatial discretization.

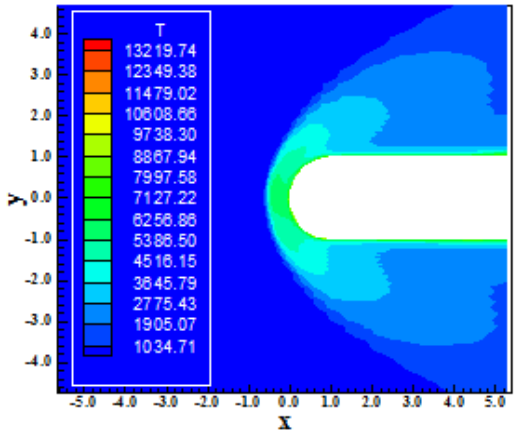

Figure 34 : Temperature contours (Mav/AS).

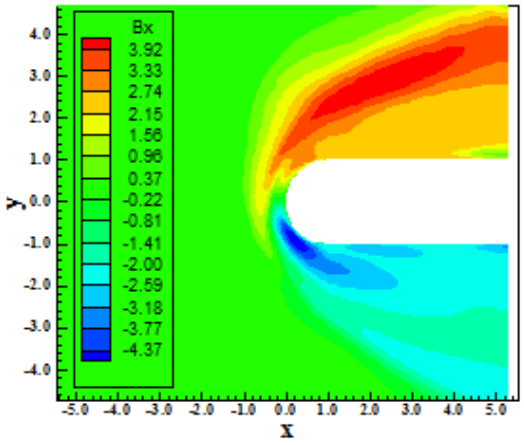

Figure 35 : B_x component of magnetic field (Mav/SS).

Figures 35 and 36 exhibit the contours of the B_x component of the magnetic field vector determined at the calculation domain. As can be observed, the B_x component is negative at the geometry lower surface and positive at the geometry upper surface, indicating that the magnetic field performs a curve around the geometry, equally observed in the solutions aforementioned. The best symmetry properties are observed in Fig. 36 (AS case).

Figures 37 and 38 exhibit the magnetic vector field with induction lines to highlight the satisfied initial condition far ahead of the configuration and the distortion in these lines close to the blunt body. As can be observed, the magnetic induction lines are initially attracted to the magnetic field imposed at the blunt body walls and, close to the body, suffer distortion, getting round the configuration. The same behavior was observed in the inviscid solutions obtained with the [10] scheme.

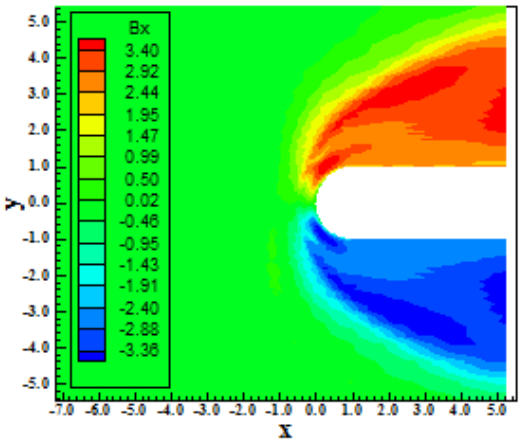

Figure 36 : B_x component of magnetic field (Mav/AS).

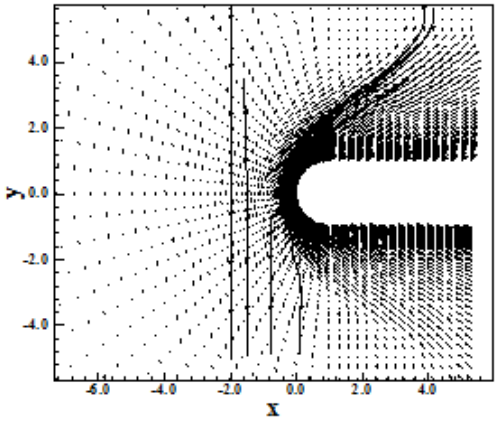

Figure 37 : Magnetic field and induction lines (Mav/SS).

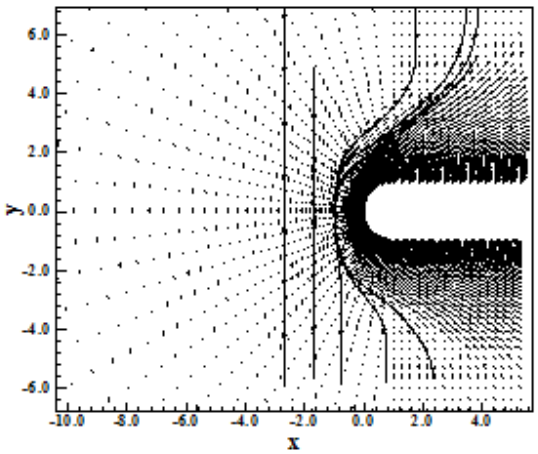

Figure 38 : Magnetic field and induction lines (Mav/AS).

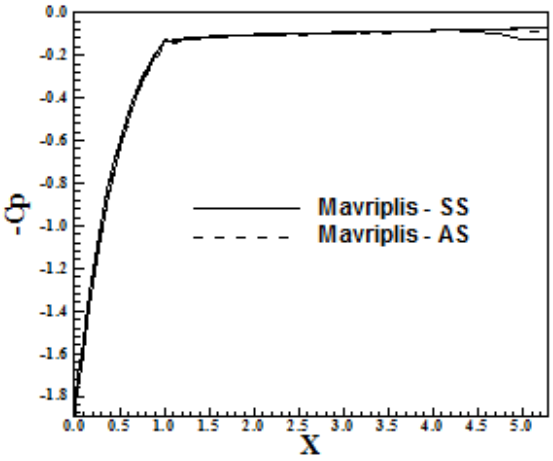

Figure 39 : -Cp distributions.

Figure 39 shows the –Cp distributions along the blunt body wall. As can be seen, the shock captured by the [10] scheme using both spatial discretizations present the same behavior.

6.5. Results to viscous flow in 2D – Azevedo operator

Figures 40 and 41 present the pressure contours calculated at the computational domain. The pressure contours obtained by the [10] scheme in the AS spatial discretization is more symmetrical than that obtained with SS spatial discretization. Again the SS solution presents a pressure peak stronger than the respective obtained in the AS case.

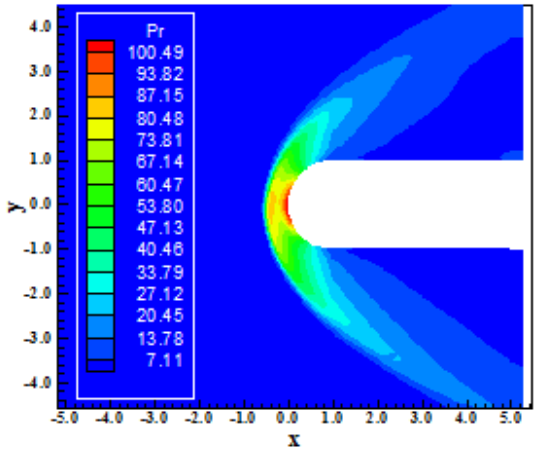

Figure 40 : Pressure contours (Az/SS).

Figures 42 and 43 exhibit the Mach number contours calculated at the computational domain by the [10] scheme employing the artificial dissipation model of [12]. The Mach number field obtained by the [10] scheme calculate at the AS spatial discretization is more symmetrical then the SS case.

It is important to note that both solutions present problems of pre-shock oscillations, being the SS discretization as more critical. Good symmetry properties are observed in the AS case.

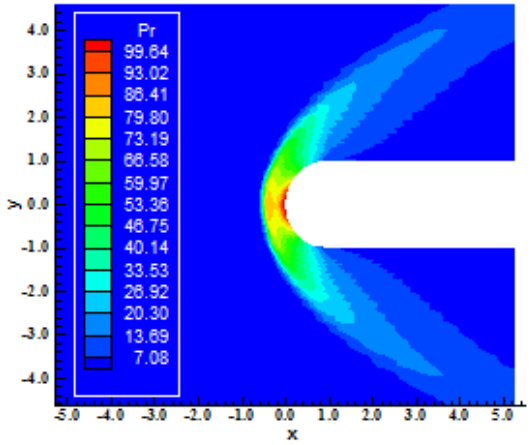

Figure 41 : Pressure contours (Az/AS).

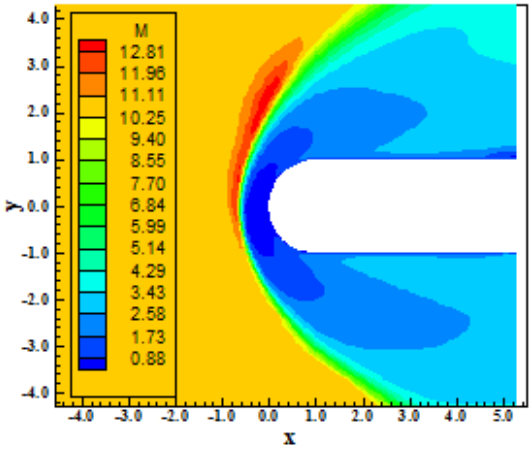

Figure 42 : Mach number contours (Az/SS).

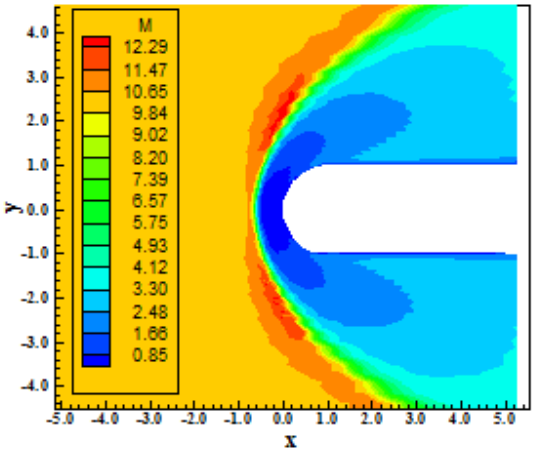

Figure 43 : Mach number contours (Az/SS).

Figures 44 and 45 show the translational / rotational temperature distributions calculated at the computational domain. The solution generated by the [10] scheme in the AS spatial discretization is more symmetrical than the SS spatial discretization. The same temperature difference is observable with the [12] dissipation model, which implies that such difference is due to the mesh discretization. As seems the AS solution is more realistic than the SS solution. The temperature peak occurs along the rectilinear walls, by the development of the heating of these by the consideration of viscous effects.

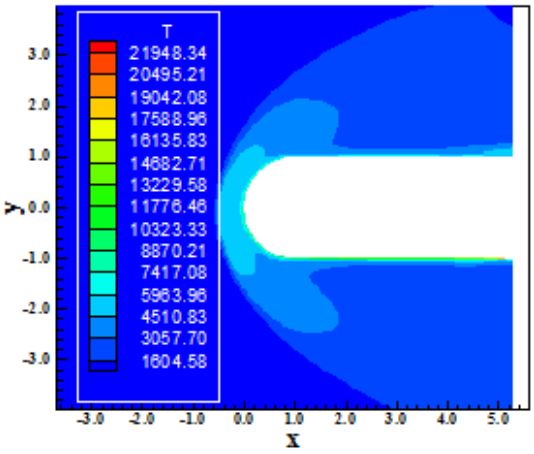

Figure 44 : Temperature contours (Az/SS).

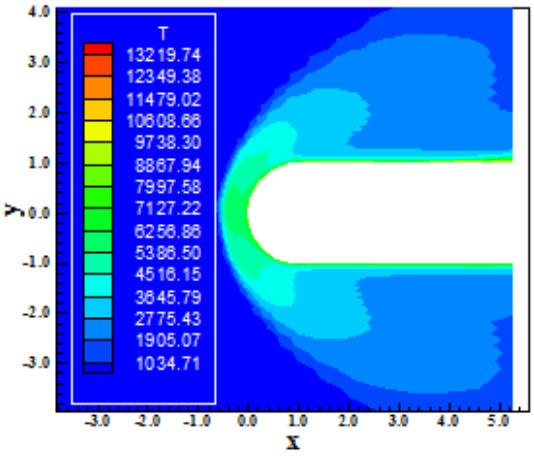

Figure 45 : Temperature contours (Az/AS).

Figures 46 and 47 exhibit the contours of the B_x component of the magnetic field vector determined at the calculation domain. As can be observed, the B_x component is negative at the geometry lower surface and positive at the geometry upper surface, indicating that the magnetic field performs a curve around the geometry. The solutions presented by the [10] scheme calculated at the AS spatial discretization have meaningful symmetry properties.

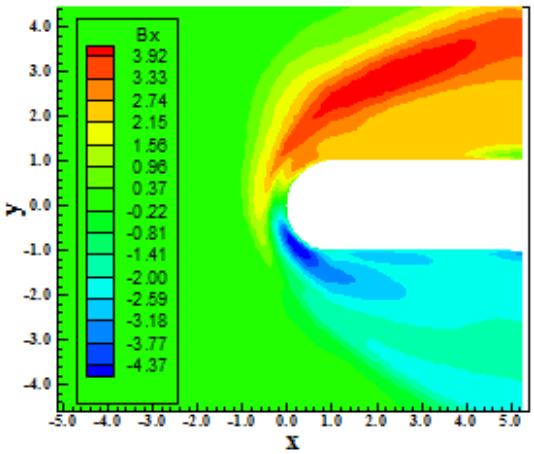

Figure 46 : B_x component of magnetic field (Az/SS).

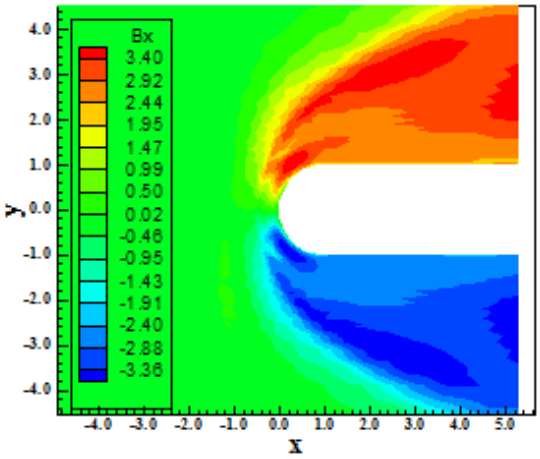

Figure 47 : B_x component of magnetic field (Az/AS).

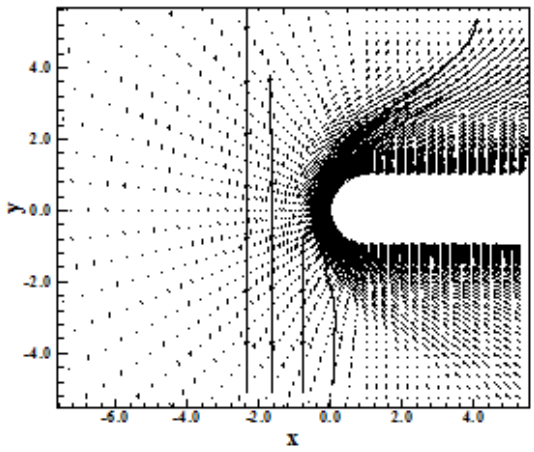

Figure 48 : Magnetic field and induction lines (Az/SS).

Figures 48 and 49 exhibit the magnetic vector field with induction lines to highlight the satisfied initial condition far ahead of the configuration and the distortion in these lines close to the blunt body. As can be observed, the magnetic induction lines are

initially attracted to the magnetic field imposed at the blunt body walls and, close to the body, suffer distortion, getting round the configuration. The same behavior was observed in the respective solutions obtained in the inviscid cases. However, the SS lines are not symmetrical, as is the case of the AS lines.

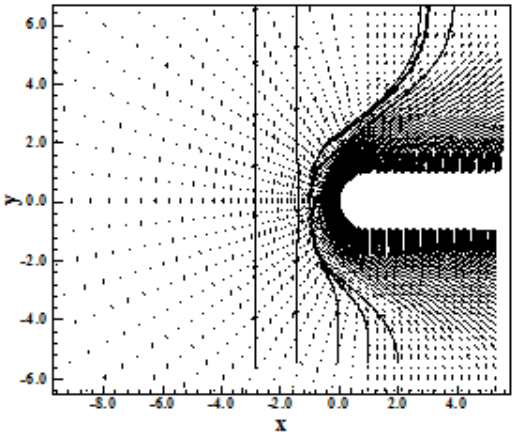

Figure 49 : Magnetic field and induction lines (Az/AS).

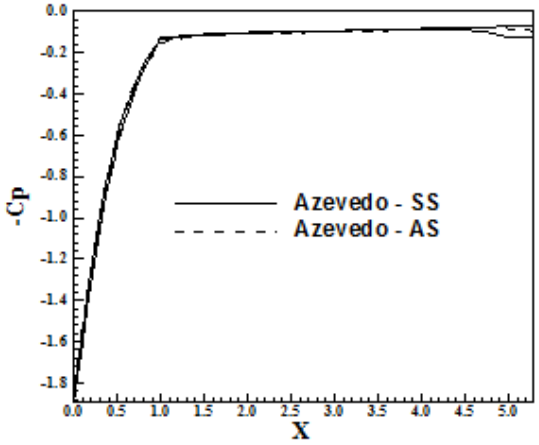

Figure 50 : -Cp distributions.

Figure 50 shows the –Cp distributions along the blunt body wall. As can be seen, the shock captured by the [10] scheme is practically the same for both spatial discretizations.

6.6. Effects of the shock standoff distance with the increase of the magnetic field vector to inviscid simulations

To these studies, the [10] scheme employing the artificial dissipation operator of [11], which presents better description of the flowfield and of the shock wave standoff distance than the [12] model, were analyzed. Variations of the $B_{y,\infty}$ component between values from 0.00T (without magnetic field influence) until 0.40T, which has presented a meaningful increase in the shock standoff distance, were simulated.

Tables 3 and 4 exhibit the shock standoff distance to each value of the $B_{y,\infty}$ component, in SS and AS cases. It is possible to conclude from these tables that the biggest shock standoff distance occurs to the maximum studied magnetic field magnitude, $B_{y,\infty}$ = 0.40T, corresponding to a distance of 1.44m, in the former case, and 1.50m in the latter case. These qualitative results accords with the literature: [26]-[27].

Table 3 : Values of normal shock standoff distance due to variations in $B_{y,\infty}$ - SS case.

$B_{y,\infty}$ (T)	X_{shock} (m)
0.00	0.95
0.05	1.38
0.10	1.38
0.15	1.39
0.20	1.39
0.25	1.40
0.30	1.40
0.35	1.42
0.40	1.44

Table 4 : Values of the normal shock standoff distance due to variations in $B_{y,\infty}$ - AS case.

$B_{y,\infty}$ (T)	**X_{shock} (m)**
0.00	1.00
0.05	1.38
0.10	1.32
0.15	1.38
0.20	1.40
0.25	1.40
0.30	1.42
0.35	1.44
0.40	1.50

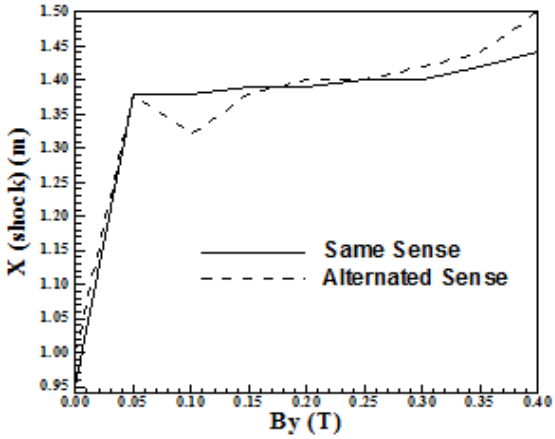

Figure 51 : Shock position as function of $B_{y,\infty}$.

Figure 51 exhibits a plot of the shock standoff distance as function of the B_y component of the magnetic field B. The values of B_y varies from 0.00T to 0.40T. As can be observed, the tendency of X_{shock} is increased as B_y increases, reducing the thermal heating which acts at the body wall. In other words, as the shock position increases, the bow shock wave is positioned far ahead of the body, reducing, hence, the intensity of the shock wave over the body. With it, the pressure and temperature fields are reduced in relation to the original shock wave, resulting in less heating and less strength of the shock wave, originating a reduction on the drag coefficient. As can be seen, the AS case presents a larger increase of the shock position.

Figure 52 shows the curves involving the iterations to convergence as function of the B_y component of the magnetic field, for the two cases of triangulation. As can be observed, exist the best value of B_y at which the convergence to the steady state condition is optimum. It occurs in both triangulations. In the SS triangulation, the optimum value is 0.35T, whereas for the AS triangulation the optimum value is 0.30T. As can be also noted, the minimum number of iterations to convergence occurs to the case B_y = 0.00T (absence of magnetic field).

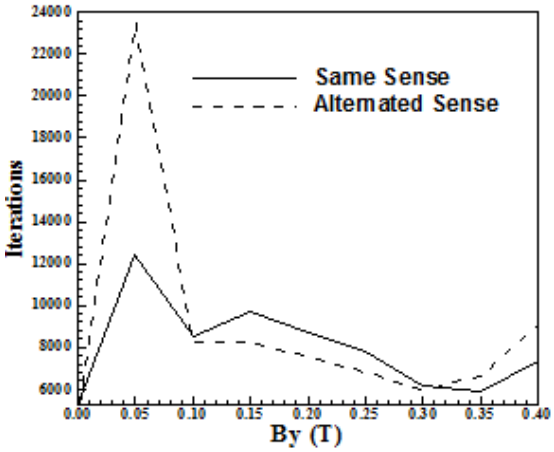

Figure 52 : Iterations to convergence as function of $B_{y,\infty}$.

6.7. Aerodynamic coefficients of lift and drag

Table 5 presents the aerodynamic coefficients of lift and drag obtained by the blunt body problem, with unstructured spatial discretization, to a formulation of ideal gas submitted to the influence of a magnetic field in two-dimensions, resulting, due to the Joule effects, in a non-ideal formulation. These coefficients take into account only the consideration of pressure term. The contribution of the friction term was not considered.

To the blunt body problem, a symmetrical configuration in relation to the x-axis, a zero value, or close to it, to the lift coefficient is expected. The solution closer to this result is due to the [10] scheme, in viscous flow, employing the SS spatial discretization and using the [11] artificial dissipation model. The maximum value of c_D was also obtained to the viscous flow, employing the [10] numerical scheme with SS spatial discretization, for both dissipation operators.

Table 5 : Aerodynamic coefficients of lift and drag to the blunt body unstructured problem.

Studied case	c_L	c_D
Inviscid/[11]/SS	-2.04×10^{-2}	0.405
Inviscid/[11]/AS	-2.56×10^{-2}	0.400
Inviscid/[12]/SS	-2.04×10^{-2}	0.405
Inviscid/[12]/AS	-2.56×10^{-2}	0.400
Viscous/[11]/SS	-2.51×10^{-4}	0.478
Viscous/[11]/AS	-7.68×10^{-3}	0.475
Viscous/[12]/SS	-2.51×10^{-4}	0.478
Viscous/[12]/AS	-7.68×10^{-3}	0.475

Table 6 presents the drag aerodynamic coefficient calculated without the influence of a magnetic field and with the presence of a magnetic field ($B_{y,\infty}$ = 0.15T). As can be observed, only the solutions obtained with the [11] dissipation operator are presented. The solutions with the [12] dissipation operator diverged. In all cases, the drag aerodynamic coefficient calculated with the presence of the magnetic field is superior in value to the same coefficient calculated without the presence of a magnetic field. This behavior is opposed to the expected. The reason for this behavior is due to the pre-shock oscillations which appear at the Mach contours, close to the body geometry. These oscillations represent strength pressure variations, which traduce in increase of the pressure field at the shock wave. So, the drag coefficient in this case is increased and becomes bigger than the same coefficients without magnetic field.

Table 6 : Comparison between drag aerodynamic coefficients.

Studied case	c_D (without B)	c_D (with B)
Inviscid/[11]/SS	0.379	0.405
Inviscid/[11]/AS	0.376	0.400
Viscous/[11]/SS	0.449	0.478
Viscous/[11]/AS	0.447	0.475

6.8. Computational performance

Table 7 presents the computational data of the simulations with magnetic field influence over a blunt body configuration in two-dimensions. The table shows the studied cases, the CFL number of the simulations, the iterations to convergence, the orders of reduction in the magnitude of the maximum residual in the field and the values of k_2 and k_4 employed in each simulation. All cases converged in three (3) orders of reduction of the maximum residual. The CFL number employed in all cases was 0.05, as also the values of $k_2 = 0.50$ and $k_4 = 0.01$. The maximum number of iterations to convergence reached less than 16,000 iterations, with the solution of the [10] scheme employing both dissipation models.

It is important to emphasize that all viscous simulations were considered laminar, without the introduction of a turbulence model, although a raised Reynolds number was employed in the simulations.

Table 7 : Computational data from the simulations with magnetic field acting on a blunt body.

Studied case	CFL	Iterations	Residual Drop	k_2 / k_4
I[(1)]/[11]/SS	0.05	9,698	3	0.50 / 0.01
I/[11]/AS	0.05	8,209	3	0.50 / 0.01
I/[12]/SS	0.05	9,698	3	0.50 / 0.01
I/[12]/AS	0.05	8,209	3	0.50 / 0.01
V[(2)]/[11]/SS	0.05	11,081	3	0.50 / 0.01
V/[11]/AS	0.05	15,980	3	0.50 / 0.01
V/[12]/SS	0.05	11,081	3	0.50 / 0.01
V/[12]/AS	0.05	15,980	3	0.50 / 0.01

[(1)]: I = Inviscid; [(2)]: V = Viscous.

Table 8 presents the computational costs of the [10] schemes in the formulation which considers the influence of the magnetic field, employing the artificial dissipation models of [11] and of [12], and considering SS and AS spatial discretization configurations. This cost is evaluated in seconds/per iteration/per computational cell. The costs were calculated employing a notebook with processor Intel Pentium Dual Core with 2.3GHz of clock and 2.0GBytes of RAM, in the Windows 7 environment.

Table 8 : Computational costs of the algorithms.

Studied case	Computational cost[(1)]
I/Mav/SS	0.0000386
I/Mav/AS	0.0000385
I/Az/SS	0.0000386
I/Az/AS	0.0000386
V/Mav/SS	0.0000892
V/Mav/AS	0.0000896
V/Az/SS	0.0000893
V/Az/AS	0.0000861

[(1)] Measured in seconds/per iteration/per computational cell.

The cheapest algorithms was the [10] scheme, in the inviscid simulation, employing the [11] artificial dissipation model, whereas the most expensive was the [10] scheme, in any other case. In the viscous case, the cheapest scheme is due to the [10] scheme, using the [12] artificial dissipation model, in a viscous calculation. The most expensive is due to the [10] scheme using the [11] artificial dissipation model, in a viscous case. In this viscous case, the former is 4.07% cheaper than the latter.

7 Conclusions

The present work aimed to implement a computational tool to simulation of inviscid and viscous flows employing a magnetic field formulation acting on a specific geometry. In this study, the Euler and the Navier-Stokes equations employing a finite volume formulation, following a unstructured spatial discretization, were solved. The aerospace problem of the hypersonic flow around a blunt body geometry was simulated. A spatially variable time step procedure is employed aiming to accelerate the convergence of the numerical schemes to the steady state solution. Effective gains in terms of convergence acceleration are observed with this technique ([13]-[14]).

The study with magnetic field employed the [10] algorithm to perform the numerical experiments. The [10] scheme is calculated by arithmetical average between the convective flux vectors at the flux interface, opposed to the arithmetical average between the conserved variable vector. The viscous flux vectors are calculated by arithmetical average of the conserved variables and of the gradients. The results are of good quality. In particular, it was demonstrated the effect that the imposition of a normal magnetic field in relation to the symmetry line of a blunt body geometry could cause the increase of the shock standoff distance, reducing, hence, the aerodynamic heating. This effect is important and can be explored in the phases of

aerospace vehicle project which does reentry in the atmosphere normal to the earth magnetic field. Another option would be the proper vehicle generates an oscillatory electrical field to yield a magnetic field in it and to induce the effect of the increase of the shock standoff distance. These are suggestions to verify.

In relation to the aerodynamic coefficient of lift reasonable values are obtained by the [10] scheme. In relation to the drag aerodynamic coefficients, none of the solutions generated by the magnetic field present values inferior to the respective ones without magnetic field. This behavior is dictated by the pre-shock oscillations that are present in Mach number contours.

The cheapest algorithm was the [10] scheme, in the viscous simulation, employing the artificial dissipation model of [12], whereas the most expensive was the [10] scheme, in the viscous simulation, employing the artificial dissipation model of [11]. In relative percentage terms, the former is 4.07% cheaper than the latter.

8 Acknowledgments

The present author acknowledges the CNPq by the financial support conceded under the form of a DTI (Industrial Technological Development) scholarship no. 384681/2011-5. He also acknowledges the infra-structure of the ITA that allowed the realization of this work.

References:

[1] P. A. Davidson, Magnetohydrodynamics in Materials Processing, *Ann. Rev. Fluid Mech.*, Vol. 31, pp. 273-300, 1999.

[2] R. W. Ziemer, W. B. Bush, Magnetic Field Effects on Bow Shock Stand-Off Distance, *Physical Review Letters*, Vol. 1, No. 2, pp. 58-59, 1958.

[3] R. X. Meyer, Magnetohydrodynamics and Aerodynamic Heating, *ARS Journal*, Vol. 29, No. 3, pp. 187-192, 1959.

[4] E. P. Gurijanov, P. T. Harsha, Ajax: New Directions in Hypersonic Technology, *AIAA Paper 96-4609*, 1996.

[5] D. I. Brichkin, A. L. Kuranov, E. G. Sheikin, MHD-Technology for Scramjet Control, *AIAA Paper 98-1642*, 1998.

[6] Y. C. Ganiev, V. P. Gordeev, A. V. Krasilnikov, V. I. Lagutin, V. N. Otmennikov, A. V. Panasenko, Theoretical and Experimental Study of the Possibility of Reducing Aerodynamic Drag by Employing Plasma Injection. *AIAA Paper 99-0603*, 1999.

[7] I. V. Adamovich, V. V. Subramaniam, J. W. Rich, S. O. Macheret, Phenomenological Analysis of Shock-Wave Propagation in Weakly Ionized Plasmas. *AIAA Journal*, Vol. 36, No. 5, pp. 816-822, 1998.

[8] E. S. G. Maciel, MGD Application to a Blunt Body in Two-Dimensions, *WSEAS TRANSACTIONS ON FLUID MECHANICS*, Vol. 7, Janeiro, Issue 1, pp. 23-47, 2012.

[9] D. V. Gaitonde, Development of a Solver for 3-D Non-Ideal Magnetogasdynamics, *AIAA Paper 99-3610*, 1999.

[10] A. Jameson, D. J. Mavriplis, Finite Volume Solution of the Two-Dimensional Euler Equations on a Regular Triangular Mesh. *AIAA Journal*, Vol. 24, No. 4, pp. 611-618, 1986.

[11] D. J. Mavriplis, Accurate Multigrid Solution of the Euler Equations on Unstructutred and Adaptive Meshes, *AIAA Journal*, Vol. 28, No. 2, pp. 213-221, 1990.

[12] J. L. F. Azevedo, On the Development of Unstructured Grid Finite Volume Solvers for High Speed Flows. *NT-075-ASE-N*, IAE, CTA, São José dos Campos, SP, Brazil, 1992.

[13] E. S. G. Maciel, Analysis of Convergence Acceleration Techniques Used in Unstructured Algorithms in the Solution of Aeronautical Problems – Part I, *Proceedings of the XVIII International Congress of Mechanical Engineering (XVIII COBEM)*. Ouro Preto, MG, Brazil, 2005. [CD-ROM]

[14] E. S. G. Maciel, Analysis of Convergence Acceleration Techniques Used in Unstructured Algorithms in the Solution of Aerospace Problems – Part II, *Proceedings of the XII Brazilian Congress of Thermal Engineering and Sciences (XII ENCIT)*, Belo Horizonte, MG, Brazil, 2008. [CD-ROM]

[15] E. S. G. Maciel, Supersonic and Hypersonic Flows on 2D Unstructured Context: Part I, *WSEAS TRANSACTIONS ON FLUID MECHANICS*, Vol. 6, October, Issue 4, pp. 199-226, 2011.

[16] E. S. G. Maciel, Supersonic and Hypersonic Flows on 2D Unstructured Context: Part II, *WSEAS TRANSACTIONS ON FLUID MECHANICS*, Vol. 6, October, Issue 4, pp. 227-256, 2011.

[17] J. C. Tannehill, D. A. Anderson, R. H. Pletcher, *Computational Fluid Mechanics and Heat Transfer*, Second Edition, Hemisphere Publishing Corporation, 792p, 1997.

[18] A. Jameson, W. Schmidt, E. Turkel, Numerical Solution for the Euler Equations by Finite Volume Methods Using Runge-Kutta Time Stepping Schemes. *AIAA Paper 81-1259*, 1981.

[19] R. C. Swanson, R. Radespiel, Cell Centered and Cell Vertex Multigrid Schemes for the Navier-Stokes Equations, *AIAA Journal*, Vol. 29, No. 5, pp. 697-703, 1991.

[20] E. S. G. Maciel, Comparação entre Diferentes Modelos de Dissipação Artificial Aplicados a um Sistema de Coordenadas Generalizadas – Parte I, *Proceedings of the 7th Symposium of Computational Mechanics (VII SIMMEC)*, Araxá, MG, Brazil, 2006. [CD-ROM]

[21] E. S. G. Maciel, Comparison Among Different Artificial Dissipation Models Applied to a Generalized Coordinate System, *Proceedings of the 8th Symposium of Computational Mechanics (VIII SIMMEC)*, Belo Horizonte, MG, Brazil, 2008. [CD-ROM]

[22] L. N. Long, M. M. S. Khan, H. T. Sharp, Massively Parallel Three-Dimensional Euler / Navier-Stokes Method, *AIAA Journal*, Vol. 29, No. 5, pp. 657-666, 1991.

[23] E. S. G. Maciel, Simulação Numérica de Escoamentos Supersônicos e Hipersônicos Utilizando Técnicas de Dinâmica dos Fluidos Computacional, *Doctoral Thesis*, ITA, São José dos Campos, SP, Brazil, 258p, 2002.

[24] R. W. Fox, A. T. McDonald, *Introdução à Mecânica dos Fluidos*, Editora Guanabara, 632p, 1988.

[25] R. W. MacCormack, The Effect of Viscosity in Hypervelocity Impact Cratering, *AIAA Paper 69-354*, 1969.

[26] H-. M. Damevin, J-. F. Dietiker, K. A. Hoffmann, Hypersonic Flow Computations with Magnetic Field, *AIAA Paper 2000-0451*, 2000.

[27] K. A. Hoffmann, H-. M. Damevin, J-. F. Dietiker, Numerical Simulations of Hypersonic Magnetohydrodynamic Flows, *AIAA Paper 2000-2259*, 2000.